

Tunable and Nacre-Mimetic Multifunctional Electronic Skins for Highly Stretchable Contact-Noncontact Sensing

Kangkang Zhou, Wangjiehao Xu, Yunfei Yu, Wei Zhai, Zuqing Yuan, Kun Dai,*
Guoqiang Zheng, Liwei Mi, Caofeng Pan,* Chuntai Liu, and Changyu Shen

Electronic skins (e-skins) have attracted great attention for their applications in disease diagnostics, soft robots, and human–machine interaction. The integration of high sensitivity, low detection limit, large stretchability, and multiple stimulus response capacity into a single e-skin remains an enormous challenge. Herein, inspired by the structure of nacre, an ultra-stretchable and multifunctional e-skin with tunable strain detection range based on nacre-mimetic multi-layered silver nanowires /reduced graphene oxide /thermoplastic polyurethane mats is fabricated. The e-skin possesses extraordinary strain response performance with a tunable detection range (50 to 200% strain), an ultralow response limit (0.1% strain), a high sensitivity (gauge factor up to 1902.5), a fast response time (20 ms), and an excellent stability (stretching/releasing test of 11 000 cycles). These excellent response behaviors enable the e-skin to accurately monitor full-range human body motions. Additionally, the e-skin can detect relative humidity quickly and sensitively through a reversible physical adsorption/desorption of water vapor, and the assembled e-skin array exhibits excellent performance in noncontact sensing. The tunable and multifunctional e-skins show promising applications in motion monitoring and contact-noncontact human machine interaction.

1. Introduction

Stretchable electronic skins (e-skins) have attracted great attention for their applications in human–machine interaction,^[1] disease diagnostics,^[2] and motion detections.^[3,4] To date, e-skins have been endowed with a variety of stimulus-sensing abilities toward strain, pressure, temperature, humidity, and various gas environments.^[5,6,7] While e-skin integrated with multiple stimulus-sensing capabilities for sensing various conditions in environment like biological skin has not been fully studied.^[8,9] In addition, numerous studies have been conducted to improve the strain detection range, sensitivity, and minimum detection limit of strain sensing e-skins.^[10,11] Wang et al. fabricated a highly stretchable e-skin to detect both large and small strains which could detect a large strain of 100% but a low gauge factor (GF) of 8741.^[12] To improve the strain sensing sensitivity of e-skin, Han et al. developed a high-performance flexible e-skin with

crack structure, achieving a high GF of greater than 5888.89, but a narrow strain range (0–2%).^[8] It remains a huge challenge to fabricate multifunctional e-skin with large response strain, high sensitivity, and low detection limit,^[13] and new strategy is urgently needed to design a new generation e-skin with desirable sensing performances.^[14,15]

Flexible conductive polymer composite with excellent flexibility and controllable conductivity, has been widely utilized to prepare strain sensing e-skins.^[16–20] Flexible polymers, including ecoflex,^[21] polydimethylsiloxane,^[22] and thermoplastic polyurethane (TPU)^[23] have been frequently used as encapsulation materials or polymeric matrix to fabricate strain sensing e-skins. For these e-skins, conductive nanofillers, such as silver nanowires (AgNWs),^[24] carbon nanotubes,^[25] reduced graphene oxides (rGO),^[26] carbon black,^[27] and metal nanoparticles,^[28] are always used to construct conductive networks. Among these nanomaterials, AgNWs with large aspect ratio have been considered as ideal candidates due to their outstanding electrical and mechanical properties and controllable nanostructures. In order to achieve a high sensitivity, as well as the ability to detect ultrahigh/ ultralow strain, a well-designed, scalable, and easily fabricated structure is essential.^[29,30] Recently, the nacre-mimetic structures have attracted extensive attention and

K. K. Zhou, W. J. H. Xu, Y. F. Yu, Dr. W. Zhai, Prof. K. Dai,
Prof. G. Q. Zheng, Prof. C. T. Liu, Prof. C. Y. Shen
School of Materials Science and Engineering
Key Laboratory of Materials Processing and Mold (Zhengzhou
University)
Ministry of Education
National Engineering Research Center for Advanced
Polymer Processing Technology
Zhengzhou University
Zhengzhou 450001, China
E-mail: kundai@zzu.edu.cn

K. K. Zhou, Dr. Z. Q. Yuan, Prof. C. F. Pan
CAS Center for Excellence in Nanoscience
Beijing Key Laboratory of Micro-nano Energy and Sensor
Beijing Institute of Nanoenergy and Nanosystems
Chinese Academy of Sciences
Beijing 101400, P. R. China
E-mail: cfpan@binn.cas.cn

Prof. L. W. Mi
School of Materials and Chemical Engineering
Zhongyuan University of Technology
Zhengzhou, Henan 451191, China

 The ORCID identification number(s) for the author(s) of this article can be found under <https://doi.org/10.1002/sml.202100542>.

DOI: 10.1002/sml.202100542

proved to have great potential in structural adjustability with excellent stability.^[31–33]

On the other hand, noncontact sensing e-skins are quite important for human health and safety in many cases and have application prospect in artificial intelligence.^[34,35] Humidity sensing has been shown to have great potential in noncontact sensing.^[36,37] Large specific surface area materials are always used to fabricate excellent humidity sensing devices because they can sense water vapor in the environment effectively.^[38,39] Moreover, rapid physical water absorption and dehydration capacity of sensing materials are critical to the reusability and response time of humidity sensors.^[40,41] 2D materials such as rGO have large specific surface area and excellent hydrophilicity, which is considered as a good candidate in humidity sensing.^[42,43]

In the present work, we fabricate a tunable and nacre-mimetic multifunctional e-skin for ultra-sensitive contact (strain sensing) and noncontact (humidity sensing) sensing based on multilayered AgNWs/rGO/TPU mats. Here, TPU electrospun mat is selected as the substrate and encapsulating material for our e-skin on the basis of their high stretchability, light weight, and skin compatibility. We use the AgNWs/rGO synergic conductive network combined with the TPU mat to construct a layer-by-layer nacre-mimetic structure. The detection range is tuned by designing the number of the conductive layers and the rGO content. Cracks are generated when the AgNWs/rGO conductive network is stretched, resulting in a high sensitivity. AgNWs tend to bridge the cracks under small strain, counteracting the unstable resistance changes caused by the rapid growth of the cracks, which greatly improves the sensing stability. Through these ingenious structural designs, our e-skin shows tunable detection range, ultralow response limit, high sensitivity, fast response time, and excellent stability in strain sensing, as well as quick and sensitive noncontact humidity sensing. Experimental observations on human such as full range human motion monitoring, respiratory monitoring and noncontact sensing array detections are applied by assembling our e-skins, satisfactory results show promising prospects in health monitoring and human machine interaction.

2. Results and Discussion

2.1. Structural Configuration

The tunable and nacre-mimetic multifunctional e-skin is fabricated by electrospinning and spray technology, the details are described in the Experimental Section. The e-skin can serve as contact sensing system to monitor human motion in real time as shown in Figure 1a. In Figure 1b, its ability to monitor humidity is a new strategy for noncontact sensing systems. Inspired by the “brick and mortar” layered architecture of nacre, the equipment diagram and the schematic illustration of fabricating the e-skin are shown in Figure S1, Supporting Information, and Figure 1c, respectively: i) A 20 μm-thick TPU mat is first prepared by electrospinning. ii) High quality AgNWs and rGO sheets (the average size of a rGO sheet is 1.1–1.5 μm), which are evenly dispersed in ethanol, are sprayed onto the prepared TPU mat. The morphologies of AgNWs and rGO used

in this work are displayed in Figures S2 and S3, respectively, Supporting Information. The AgNWs with various lengths (70.5–1377 μm) play a crucial role in constructing excellent conductive networks. iii) Another layer of TPU mat is prepared to cover the conductive AgNWs/rGO. iv) Different AgNWs/rGO conductive layers and TPU layers are designed layer by layer to imitate the nacre structure to construct e-skins.

The morphology of e-skin with 8-layer of AgNWs/rGO conductive network is studied as shown in Figure 1d–f. As shown in Figure 1d, TPU fibers with smooth surface and a diameter of 3 μm are randomly distributed. Figure 1e shows the morphology of AgNWs/rGO layer after the spraying process. The AgNWs and overlapping rGO are evenly distributed across the TPU mats. A synergic AgNWs/rGO conductive network is constructed successfully on the TPU fibrous mats. Figure S4, Supporting Information, and the illustration in Figure 1e display the energy dispersive spectrometer (EDS) mapping images of different elements in AgNWs/rGO layer, showing that conductive fillers are evenly distributed. The nacre-mimetic e-skin employs hydrophilic 2D rGO nanosheets and highly conductive 1D AgNWs as the “brick” and TPU mats as the “mortar”, which is constructed by electrospinning method. As shown in Figure 1f, cross-section scanning electron microscopy (SEM) confirmed that the conductive layers are staggered with the TPU mats layer by layer, exhibits representative nacre-mimetic layered architecture. In this structure, the rGO-AgNWs “brick” endows the system with high electrical conductivity and mechanical brittleness, and the TPU mats “mortar” increases flexibility by interfacial interactions, nanofibers stretching, and layer slippage. Due to the nacre-mimetic structure of good mechanical robustness, our e-skin can work in a large strain range (0–200%) and work normally after 11000 cycles of stretching-releasing tests. The thickness of 120 μm ensures the air permeability and wearing comfort of the e-skin. Our e-skin can be stretched, twisted, and bended easily, showing excellent flexibility (Figure S5, Supporting Information). As contrasts, single rGO and single AgNWs fillers are also used to prepare multilayered fibrous mats, respectively. Figure S6, Supporting Information, depicts the cross-sectional SEM images of the rGO and AgNWs decorated TPU fibrous mats, respectively. It can be seen that the conductive networks constructed by single AgNWs without rGO are relatively poor.

Thermogravimetric analysis (TGA) of pure TPU nanofiber mats and the e-skin is performed to investigate the filler concentration and thermal stability of the material. Here, the conductive filler content is calculated through the formula as follows:^[44]

$$m_i = m_s + m_p \quad (1)$$

$$bm_i = m_s + am_p \quad (2)$$

where m_i , m_s , and m_p represent the weight of the e-skin, conductive filler, and TPU mats, respectively; a and b are the weight ratios of the residual of e-skin and TPU nanofiber mats, respectively. Based on these formulas, the conductive filler content ω_s in e-skin is calculated:

$$\omega_s = \frac{m_s}{m_i} = \frac{b-a}{1-a} \quad (3)$$

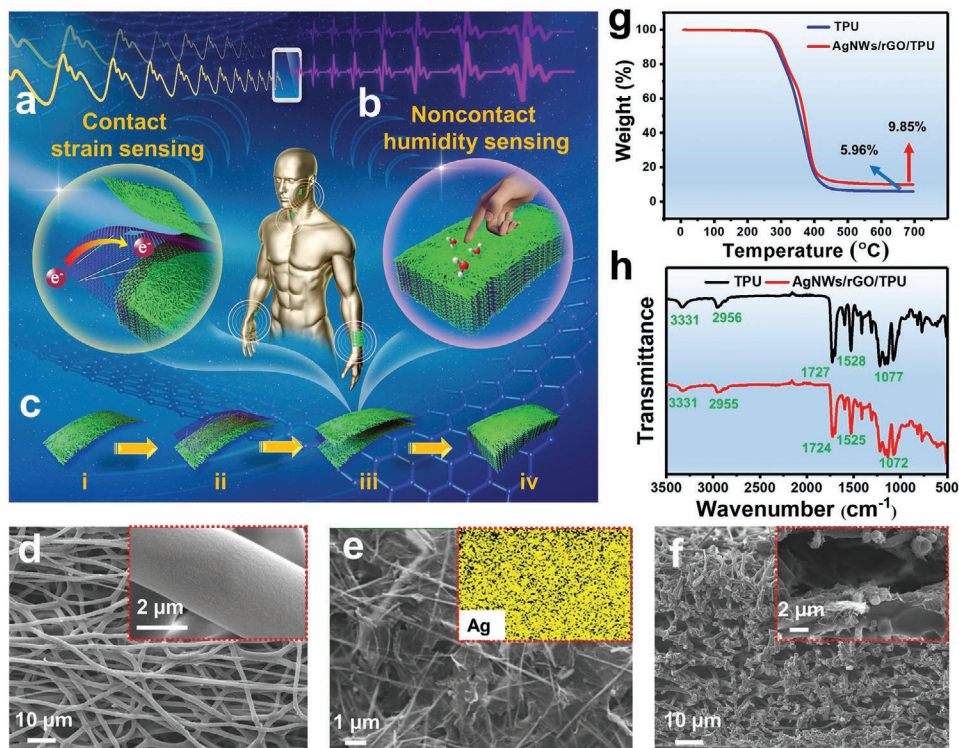


Figure 1. The e-skin serves as a) contact sensing system and b) noncontact sensing array. c) The fabrication process of e-skin. d) Surface SEM images of the e-skin. e) SEM and EDS mapping images of the AgNWs/rGO conductive network of the e-skin. f) Cross section SEM images of the e-skin. g) TGA and h) FTIR curve of pure TPU mats and the e-skin.

As shown in Figure 1g, weight ratios of the residual for e-skin and TPU nanofiber mats are 9.85% and 5.96% at 700 °C, respectively, so the ω_s is calculated to be 4.1%. Moreover, the TGA curve of e-skin shifts toward the high temperature zone, indicating that the conductive filler has been adhered to the surface of the nanofiber, which can also be observed in Figure 1e. Furthermore, the Fourier transform infrared (FTIR) spectra of our e-skin and pure TPU nanofiber mats are tested to investigate the chemical interaction between conductive filler and TPU. After AgNWs/rGO is sprayed on the TPU nanofiber surface, the absorption peaks at 3331, 2956, 1727, 1596, and 1077 cm^{-1} (belong to N–H stretching band, –CH stretching vibrations, –H–N–CO–, N–H, and C–O–C bands, respectively) shift to 3326, 2948, 1723, 1521, and 1074 cm^{-1} , respectively (Figure 1h). The changes in the peaks demonstrate that chemical interactions exist between conductive filler and polymer chains. It is beneficial to the decoration of conductive filler on TPU nanofiber surface to form excellent conductive paths.

2.2. Tunable Contact Sensing Capability of the E-Skin

Two ends of the e-skin are coated with silver paste and each layer in e-skin-8 is bonded with silver pastes at the end of the e-skin. Then e-skin-8 was attached to the copper tape as electrodes for electrical properties tests (Figure S7, Supporting Information). Obviously, the conductive layers are connected in parallel because the TPU fibrous mats are permeated by the silver paste. It is worth noting that the conductive layers are

isolated from each other by the TPU layers, which restrict electron transport perpendicular to the e-skin. The resistivity of the e-skins with 1, 4, 6, and 8 conductive layers are 181.2, 50.4, 37.6, and 28.7 $\Omega\text{-cm}$, respectively, as shown in Figure S8, Supporting Information, which are close to the calculation result of a parallel circuit. The contact strain sensing capability of the e-skin can be tuned by changing rGO content in AgNWs/rGO (0, 14.3, 20, 33.3, 50, 66.7, and 100 wt%). Here, the different e-skins with varying rGO content are represented by e-skin-0, e-skin-14.3, e-skin-20, e-skin-33.3, e-skin-50, e-skin-66.7, and e-skin-100, respectively. The strain sensing capability of the e-skins with different rGO contents is studied toward the strain at a tensile rate of 10 mm min^{-1} as shown in Figure 2a. It can be seen that the relative resistance change ($\Delta R/R_0$, where R_0 is the original resistance, R is the resistance under strain, $\Delta R = R - R_0$) decreases with the increase of rGO content. The $\Delta R/R_0$ value of e-skin-0 increases drastically to 15 at only 3% strain (the highest $\Delta R/R_0$ compared with the other samples at the strain), showing that e-skin-0 has great advantages in detecting small strain with a high sensitivity. For other e-skins (e-skin-14.3, e-skin-20, e-skin-33.3, e-skin-50, e-skin-66.7, and e-skin-100), the strain detection ranges are 48%, 50%, 69%, 135%, 160%, and 200%, respectively. It is worth noting that the maximum detection strain here represents a complete failure of conductive layer in the e-skin rather than a sample rupture. Obviously, a higher rGO content, which is beneficial to constructing a better conductive network, results in a lower responsivity and a large responsive range toward the same strain/stress stimuli. While e-skins containing higher ratio of AgNWs exhibit excellent

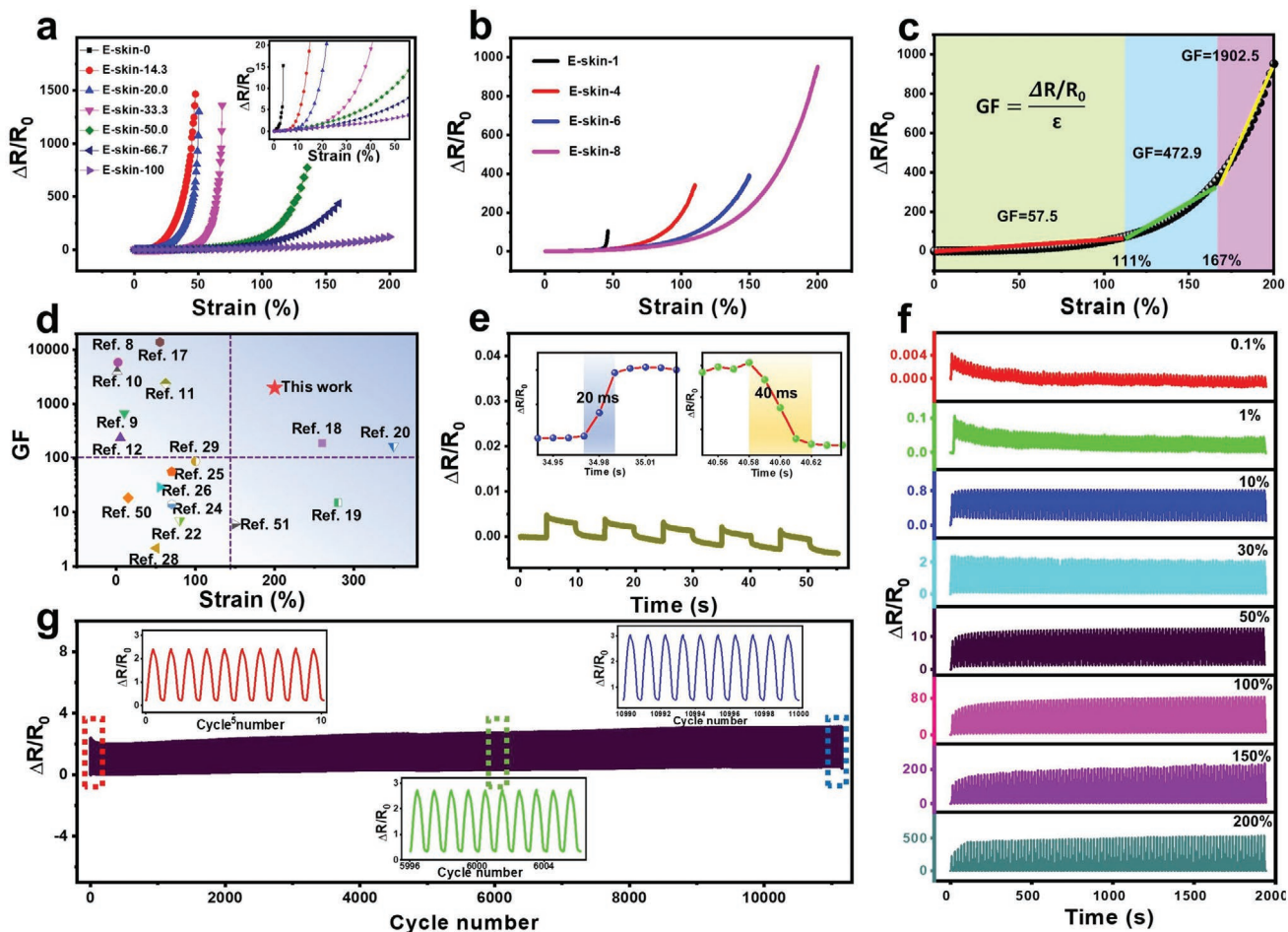


Figure 2. a) $\Delta R/R_0$ –strain curve with different content of rGO in the synergic conductive network. b) $\Delta R/R_0$ –strain curve of our e-skin with different conductive layers. c) GF of e-skin-8. d) A summary graph of GF of e-skin-8 and other reported e-skins at maximum tensile strain. e) Response and recovery time of the e-skin. f) $\Delta R/R_0$ variation of e-skin-8 at diverse maximum strains of 0.1–200% in 100 stretching-releasing cycles. g) 11 000 stretching/releasing cycles toward 30% strain (the inserts are sensing behaviors during 1–10, 5996–6006, and 10 990–11 000 cycles, respectively).

sensitivity over a small strain range, showing tunable sensing properties. In addition, the strain sensing capability of e-skin can also be adjusted by designing the number of conductive layers, they are represented by e-skin-1, e-skin-4, e-skin-6, and e-skin-8 (1, 4, 6, and 8 layer, the weight ratio of rGO to rGO/AgNWs is 50%), respectively. In Figure 2b, the strain sensing ranges of these e-skins increase from 46 to 200% gradually. The results show that our e-skin can be tuned to satisfy the requirements of different deformation detection, which is important for high precision detection.^[45]

E-skin-8 is selected for the further test based on its large strain detection range. The changes of stress as a function of strain of pure TPU mats and e-skin-8 are depicted in Figure S9a, Supporting Information. The elongations of break of the two materials are 622.4% and 581.8%, respectively, showing an ultra-high stretchability. The low elastic modulus (10.9 MPa) of e-skin-8 is favorable for the application of wearable e-skin. E-skin-8 shows lower modulus after repetitive stretching-releasing due to the rearrangement of fibrous network and TPU macromolecular network. As shown in Figure S9b, Supporting Information, the hysteresis phenomenon is not obvious at low

strains. The strain sensing performances of e-skin-8 toward tensile stress are then investigated. As displayed in Figure S10a, Supporting Information, $\Delta R/R_0$ of e-skin-8 increases monotonically with strain, and it is obvious that a wide response range (0–200%) has been achieved for our e-skin-8. The slope of the $\Delta R/R_0$ –strain curve increases in three regions: I) slow increase region; II) steady increase region; III) rapid increase region (region I 0–111%, II 111–167%, and III 167–200%). We carried out the linear fitting to the three-part curve (Figure S10b–d, Supporting Information). Results show that the $\Delta R/R_0$ –strain curves conform to the linear rule in each region, and the slope (GF) and R^2 values in different regions are 57.5, 472.9, 1902.5 and 0.902, 0.967, 0.985, respectively. The sensitivity of the strain sensing capability is evaluated by using the GF:^[46]

$$GF = \frac{\Delta R/R_0}{\varepsilon} \quad (4)$$

where ε is the strain in tension. The sensitivity is then calculated by using the linear simulation with the GF of 57.5, 472.9, and 1902.5 in region I, II, and III, respectively. Attributed to the

evolution of the AgNWs/rGO network, a typical curve of the change tendency of $\Delta R/R_0$ is shown in Figure 2c. The conductive paths are broken partially due to the generation of cracks when subjected to strain. However, the bridge structure by AgNWs counteracts the damage of the cracks in the conductive network, leading to a facile increase in GF (region I, the orange region). With the increase of strain, the cracks expand, leading to a decrease in the number of conductive paths and an increase in resistance (region II, the blue region). When the strain is further increased, cracks form island structure due to the continuous expansion, resulting in the sharply increased GF (region III, the green region). As mentioned above, a large workable range together with a high sensitivity are still a huge challenge for a satisfactory e-skin.^[47] As shown in Figure 2d, our e-skin-8 has achieved satisfactory comprehensive performance (GF is 1902.5 at maximum strain of 200%) compared to the reported literatures.^[8–12,17–20,22,24–26,28,29,50,51]

Rapid response certainly helps to monitor human health indicators in real time.^[48] A subtle stretching (0.1% strain) is loaded on a sample at a rate of 1000 mm min⁻¹. A response time of 20 ms and a recovery time of 40 ms are obtained for our e-skin-8, which are faster than most of the reported sensors and our previous researches (Figure 2e).^[8,10,12,20,22] The response time of the single rGO based 8-layer conductive network e-skin is slower (90 ms) as shown in Figure S11, Supporting Information. It thus deduces that the response time of our e-skin-8 has been greatly shortened due to the addition of AgNWs with a large aspect ratio but few contact points.

Figure S12, Supporting Information, exhibits the current–voltage characteristic curves of e-skin-8 under diverse strains (0%, 10%, 30%, 50%, 100%, 150%, and 200%), which follows the Ohm's law exactly. The good linearity of the curve under various voltages indicates that the strain sensor has excellent reliability under a wide strain range. Cyclic stretching–releasing tests toward different strains (0.1–200%) are also performed. As presented in Figure 2f, the superb repeatability demonstrates that the e-skin-8 has good stability and excellent strain sensing discernibility in a large sensing range, even in the first five stretching/releasing cycles (Figure S13, Supporting Information). Reliable response at different operating frequencies is also important for complex applications. Sensing behaviors of e-skin-8 toward various tensile rates (30% strain) are then studied (Figure S14, Supporting Information). The similarity of the peaks indicates that the effect of varying tensile rates on the relative resistance is weak. Excellent long-term performance is important for the practical application of e-skin, which can reduce the cost and enlarge the popularity remarkably.^[49] In Figure 2g, it is found that the stability and repeatability of e-skin-8 are excellent even after 11000 stretching/releasing cycles, exhibiting remarkable durability in long-term and frequent use. The changes of $\Delta R/R_0$ during 0–10, 5996–6006, and 10990–11000 cycles are shown in the insets of Figure 2g specially, also showing excellent sensing durability. Stress–strain curves of e-skin-8 in different cycles are displayed in Figure S15, Supporting Information, it is found the residual strain of e-skin-8 is quite small in long-term use, which is mainly related to the designed nacre-mimetic structure and the good binding between AgNWs/rGO conductive network and TPU fibers.

The sensing behavior toward bending of e-skin is equally important. E-skin-8 is then attached on a polycarbonate (PC) film (thickness of 1 mm) as shown in Figure S16, Supporting Information. To evaluate the sensing behaviors toward bending clearly, we define the bending angles by a concise formula:

$$\Delta\varepsilon = \frac{\Delta L}{L_0} = \frac{L_0 - L}{L_0} \quad (5)$$

where L_0 is the original length of the film ($L_0 = 15$ mm), L is the chord length. Our e-skin-8 exhibits ideal resistance responses toward varying bending deformations (0–80%) as shown in Figure S16, Supporting Information. The sensing behaviors toward bending in 5 bending–releasing cycles are performed under different $\Delta\varepsilon$ (Figure S17, Supporting Information), which demonstrates that bending sensing of the e-skin could work stably in various deformations (0–80%). In order to evaluate the bending durability, 1000 bending–releasing cycles are also investigated at a $\Delta\varepsilon$ of 30%. The similar shape of the curves reveals remarkable repeatability of the bending sensing performance of the e-skin-8 (Figure S18, Supporting Information).

2.3. Working Mechanism and Modeling Study of Strain Sensing

Figure S19, Supporting Information, illustrates the morphology change of the conductive layer under different strains, which shows the generation and expansion of cracks in the conductive network. Due to the slippage of the nanofibers in the TPU mats, our e-skin cannot fully recover to its original length after unloading the stress. Residual strain leads to tiny cracks and wrinkles in the rGO/AgNWs conductive layer after reconstruction, which causes the slight increase in resistance (Figure S19f, Supporting Information). It is worth mentioning that when the reconstructed conductive layer is stretched again, its minimum resistance in each cycle does not change significantly, and the strain response performance becomes more stable. As shown in **Figure 3**, three representative strains were selected to explain the evolution of the conductive network structure in various regions: 50% strain represents region I (0–111% strain); 150% strain represents region II (150–167% strain) and 200% strain represents region III (167–200% strain). The crack width increases rapidly from 10 to 80 μm as the tensile strain increases from 50 to 200%. The evolution of the conductive network can be divided into bridge structure, crack structure, and island structure, respectively. Conductive paths are broken partially owing to the generation of cracks at 50% strain (Figure 3a,b, region I). AgNWs with various lengths bridge structure counteracts the damage of the cracks as presented in Figure 3b, ensuring the efficient electronic transmission. As the strain increases to $\approx 150\%$ strain (region II), the cracks propagate, leading to a gradual decrease in the number of conductive paths (Figure 3c,d). When the strain is further increased up to 200% as displayed in Figure 3e,f (region III), the cracks are extended obviously to form the island structures due to the continuous expansion.^[50]

The morphology development of conductive fillers on the conductive network toward different strains is simulated in Figure 3g–i. In region I, the conductive paths are

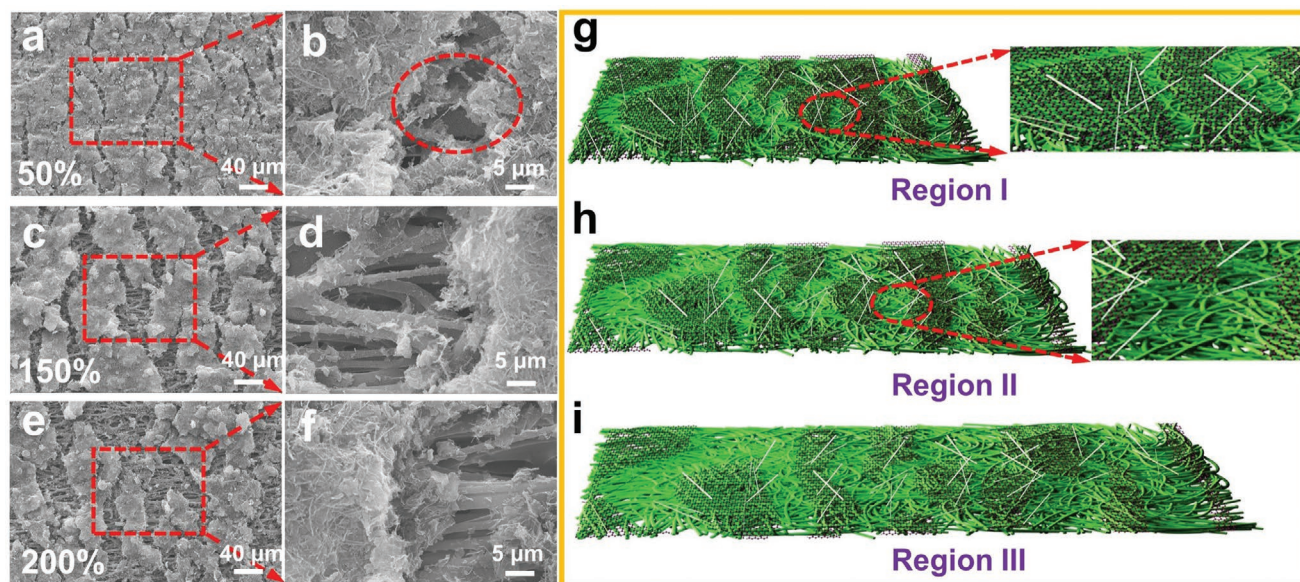


Figure 3. a–f) Surface SEM images of the AgNWs/rGO conductive layer of e-skin under various strain. g–i) Schematic diagram of simulated single-layer conductive network in different tensile stages in region I, II, and III.

broken partially because of the generation of small cracks (Figure 3g). Some cracks (width $\leq 10 \mu\text{m}$) are bridged by AgNWs with large aspect ratio, maintaining the residual conductive pathways. The introduction of AgNWs prevents the conductive network from being damaged sharply. As a consequence, e-skin-8 exhibits excellent strain sensing stability compared with other crack based e-skins. In region II, as the strain increases, the width and quantity of cracks increase obviously (Figure 3h), which breaks the bridge structure, resulting in the hindered electron transfer. In region III, the width of cracks increases sharply (more than $100 \mu\text{m}$), causing an obvious reduction in the number of electrical pathways (Figure 3i).^[51]

2.4. Noncontact Sensing Capability of the E-Skin

Noncontact sensing has a wide application in privacy protection, disease isolation, and some hazardous environments; humidity detection is a simple and effective way of noncontact sensing.^[51] As shown in Figure 4a, with the rise of relative humidity (RH), $\Delta R/R_0$ of our e-skin-8 also increases gradually and rapidly, showing excellent resolution to different RH. It is worth mentioning that as the RH decreases, $\Delta R/R_0$ decreases and almost returns to its original state, showing good sensing recoverability. In Figure 4b, the response and recovery of e-skin-8 at different RH are tested in five cycles to evaluate the response stability, the smooth curves, and similar peaks demonstrate the excellent stability of e-skin. Figure 4c displays the variation of $\Delta R/R_0$ in different RH environments, $\Delta R/R_0$ increases almost linearly as RH rises. In order to quantitatively characterize the relationship between resistance and humidity, we fit the curves of humidity and resistance via Equation (6).

$$\gamma = 0.05x - 0.2 \quad (6)$$

where γ is $\Delta R/R_0$ and x is RH, here, the R^2 achieve 0.97. Obviously, by using this equation, the RH value can be predicted based on the tested $\Delta R/R_0$ value. To predict the indoor RH, we exposed the e-skin to the air and measured the $\Delta R/R_0$, the value was 1.98 as shown in Figure 4d. We then calculated the RH to be 43.6% through the equation. It is very similar to the actual indoor humidity (44% RH), indicating that our e-skin has a high accuracy in humidity sensing.

As shown in Figure 4e, the randomly distributed TPU fibers form porous mats, the water molecules can thus pass unimpededly and contact with rGO efficiently. rGO has a high specific surface area and some hydrophilic groups, such as carboxyl groups, which endows the e-skin-8 with the capability of capturing water molecules facily from the external environment.^[52] At a low RH, rGO shows *p*-type conductive behaviors controlled by holes.^[53] Water molecules absorbed by rGO lead to a decrease in the number of holes in the rGO, which reduces the conductivity of the conductive network.^[54] At a high RH, large number of water molecules produce hydronium ions, which act as conductive carriers to improve the conductivity of rGO to some extent.^[55] On the other hand, lots of water molecules induce swelling effect of the multilayer TPU mats, increasing the distance between the conductive fillers and decreasing the electrical conductivity of our e-skin.^[56] Under the trade-off of swelling effect and hydronium ions, the conductivity of the e-skin decreases at high RH.^[57]

Figure 4f shows the current–voltage characteristic of e-skin-8 under diverse RH. With the increase of voltage, the current of e-skin-8 rises smoothly with the increase of RH. The current of e-skin-8 in high RH environment is less than that in low humidity environment, which follows the Ohm's law exactly and shows excellent resolution. In view of the high sensitivity and quick response ability of our e-skin-8, it was fitted to outer surface of the mask to measure the relative humidity of human respiration as shown in Figure 4g. According to the

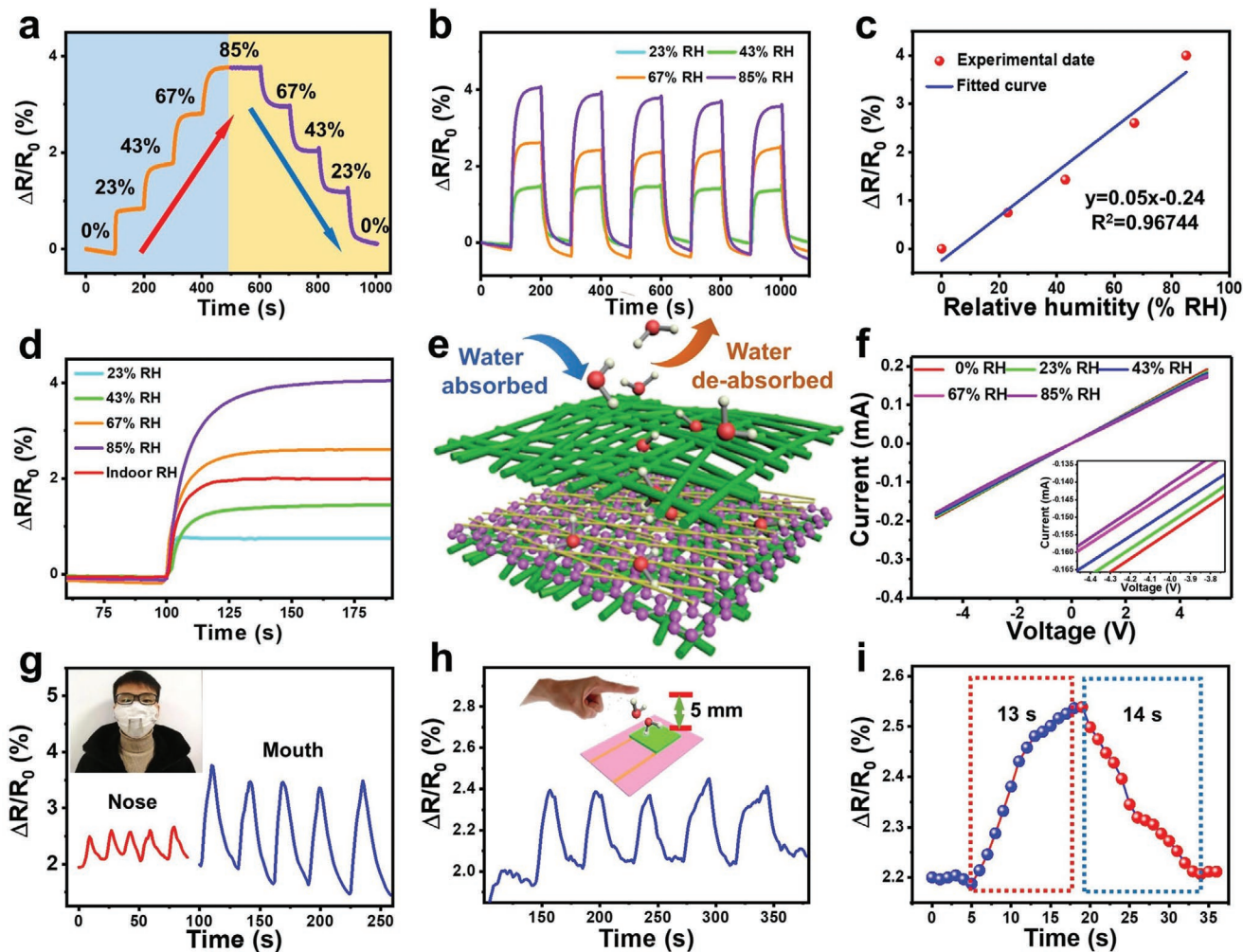


Figure 4. a) $\Delta R/R_0$ of e-skin-8 under various RH. b) 5 cycles of $\Delta R/R_0$ and RH variation. c) Normalized response of e-skin-8 as a function of RH. d) The $\Delta R/R_0$ of indoor RH compared with the $\Delta R/R_0$ toward different RH. e) Schematic diagram of e-skin's response to humidity. f) I–V curves of e-skin-8 with diverse RH. g) e-Skin-8 monitoring of human breath by nose and mouth. h) The monitoring of the humidity around the fingers. i) The response time of e-skin-8 to humidity.

formula, the RH of the volunteer breathing through his nose was 54% RH and that of the volunteer breathing through his mouth was 78% RH. It is worth noting that the temperature and relative humidity of the test room were 27.2 °C and 47%, respectively. In such test room, the relative humidity around the volunteers' fingers was slightly higher than the RH in the air. As shown in Figure 4h and Movie S1, Supporting Information, our e-skin-8 can sense the RH of a finger at a distance of 5 mm, which demonstrates the application prospect in the field of noncontact control system. Figure 4i shows that our e-skin has the ability to detect humidity quickly and sensitively, which shows a potential in non-contact sensing. Due to the different response time of strain sensing and humidity sensing (20 ms in Figure 2e and 13 s in Figure 4i), the response curves of e-skin to different stimuli are also different, which can be used to identify the source of the signal when e-skin-8 works in both modes.

2.5. Applications of the E-Skin

Our tunable and nacre-mimetic multifunctional e-skins show great application prospect in human motion monitoring and wearable noncontact sensing system. In human movement monitoring, the excellent sensitivity, large strain response range and excellent durability endow our e-skin-8 with good capacity of detecting various mechanical signals generated by human motions. As depicted in Figure S20a–c, Supporting Information, e-skin-8 is attached to the joints of the upper limbs. We can clearly distinguish the motion signals of different parts. It is worth noting that our e-skin-8 is able to distinguish the finger, wrist, and elbow bending with different angles (30°, 60°, and 90°) (Movies S2–S4, Supporting Information). The assembled e-skin-8 for human sport monitoring is shown in Figure 5a. Our samples are attached to both wrist and elbow when playing badminton, which exhibits excellent

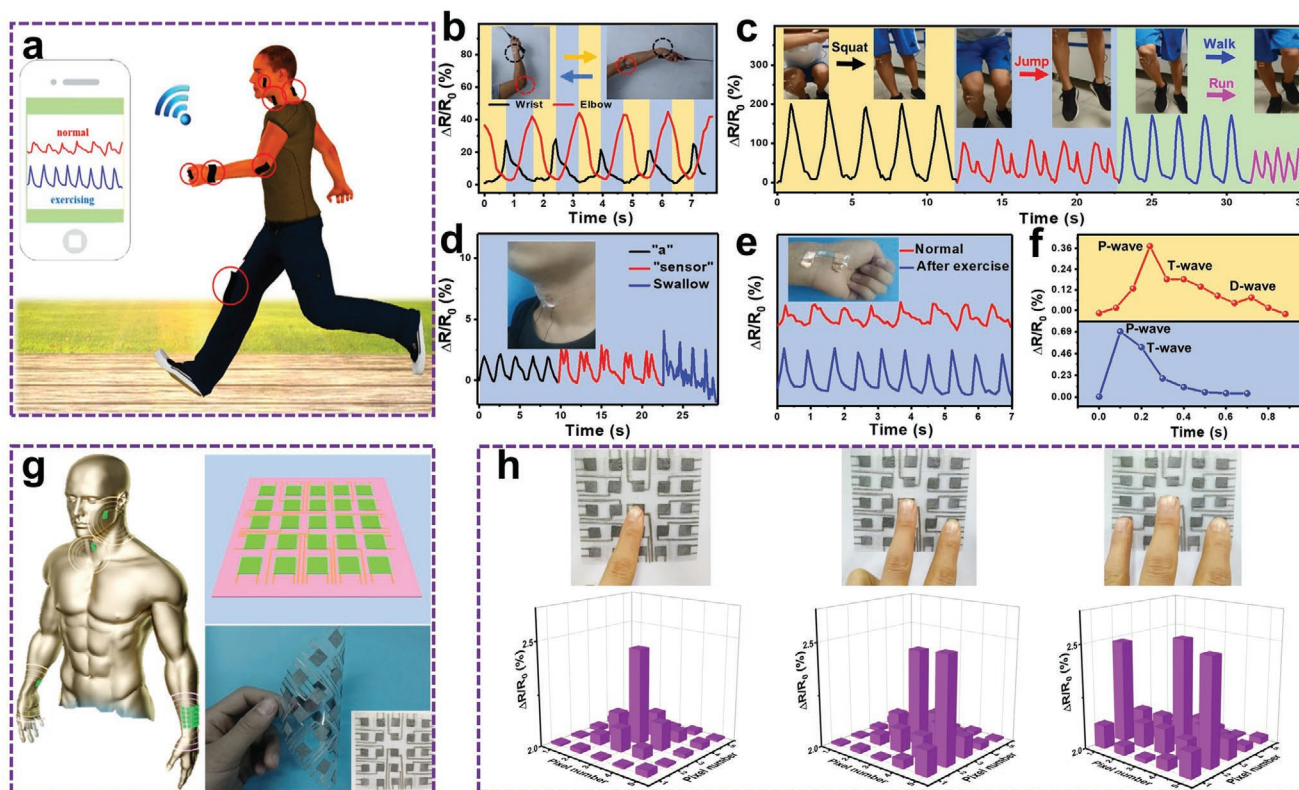


Figure 5. a) Applications of the e-skin in full-range human motion monitoring. b) Motion detection for playing badminton. c) Responses of e-skin-8 toward cyclic motions: squatting, jumping, walking, and running. d) Responses of e-skin-8 assembled on the throat to monitor Adam's apple vibration. e) Real-time monitoring of adult wrist pulse. f) The magnified view of wrist pulse signals. g) Applications of the e-skin in noncontact sensing system. h) E-skin-8 array sensing of fingers' RH and distribution (noncontact mode).

synchronization and stability (Figure 5b). Figure S20d, Supporting Information, presents the sensing performance of our e-skin toward leg lifts (Movie S5, Supporting Information). In Figure 5c, e-skin-8 is assembled on a knee of volunteer, various motions such as jumping, squatting, walking, and running can be detected well by distinguishing the sensing amplitude and frequency (Movies S6 and S7, Supporting Information).

Additionally, we found e-skin-8 possesses excellent potential applications in small-scale motion monitoring. The samples are assembled on the volunteer's cheek and hind neck as shown in Figure S21, Supporting Information, the $\Delta R/R_0$ shows discernible values when the volunteer opens his mouth, puffs out his cheek, nods and shakes his head, indicating that e-skin-8 can clearly distinguish the gentle motions. In Figure 5d, e-skin-8 is assembled onto volunteer's throat, repeatable and recognizable signals are recorded when the volunteer speaks "a", "sensor" and swallows. To monitor subtle movements, e-skin-8 is attached to the wrist to detect an adult's pulse (Figure 5e). 8 periodic pulse shapes are clearly displayed within 7 s, which is completely consistent with the pulse rate of a healthy adult ($68 \text{ beats min}^{-1}$). In addition, after the volunteer exercises for 10 min, his heart rate reaches 85 min^{-1} by analyzing the sensing signals. The detailed diagram of wrist pulse signals is depicted in Figure 5f. The signals clearly illustrate the percussion (P), tidal (T), and diastolic (D) characteristic peaks in 0.88 s, and the signals after exercising show increasing signals intensity in

0.70 s. All of these tests display the promising application of e-skin-8 in the field of full-range human motion monitoring.

Furthermore, based on the high sensitivity and excellent stability in humidity sensing of e-skin-8, it can also be applied as wearable noncontact sensing system. As shown in Figure 5g, e-skins are attached to a flexible PC film, forming a 5×5 array. For e-skin, it should be able to sense not only the intensity of external stimuli, but also the distribution of stimuli. In Figure 5h, our e-skin-8 array senses the relative humidity of the fingers precisely and keenly, the number and distribution of the fingers are also clearly recorded, demonstrating the wide range of applications of the e-skin array for noncontact sensing system. The results demonstrate that the e-skin can perform full movement monitoring of human and wearable noncontact sensing system, showing great potential in human machine interaction and artificial intelligence.

3. Conclusions

In summary, tunable and nacre-mimetic multifunctional e-skins based on multilayered AgNWs/rGO/TPU fibrous mats with contact and noncontact sensing capability are fabricated by electrospinning-spraying technique. For contact strain sensing, the strain sensing ability of the e-skin can be tuned by changing rGO content and conductive layers. The

e-skin demonstrates excellent electro-mechanical performance with very wide and tunable detection range (50–200% strain), ultra-low detection limit (0.1% strain), high sensitivity (GF of 1902.5 in 200%), fast response time (20 ms) and excellent stability (stretching/releasing test of 11000 cycles). For the sensing mechanism, rGO cracks are generated in tension/bending, the islands among gaps can be bridged by AgNWs. This novel structure leads to satisfactory sensing performances, including the high sensitivity, large workable range, and excellent stability and durability. Our e-skin-8 can detect full range human body movements (walking, playing badminton and some subtle facial movements, etc.), which has promising application in health and exercise monitoring. For noncontact sensing, our e-skin possesses high sensitivity and quick response capability, and exhibits a precise sensitivity to the RH of human breath and fingers. More importantly, the e-skin array show practical applications in noncontact sensing and control systems. All these results suggest that tunable and nacre-mimetic multifunctional e-skins possess great potential in health monitoring and contact-noncontact human machine interaction.

4. Experimental Section

Materials: rGO was purchased from Suzhou TanFeng Graphene Science and Technology Co. Ltd., China and the purity was ≈95 wt%. Silver nitrate (AgNO₃) was purchased from Sinopharm Chemical Reagent Co., Ltd., China. Poly(vinylpyrrolidone) (PVP, Mw = 1 300 000 g mol⁻¹) was obtained from Usofar Chemical Technology Co. Ltd. Tsingtao, China. TPU (code Elastollan 1185A with a density of 1.12 g cm⁻³) was provided by BASF Co. Ltd. Tetrahydrofuran (THF) and ethylene glycol (EG) were bought from Fuyu Fine Chemical Co. Ltd, Tianjin, China. N, N-Dimethylformamide (DMF) and sodium chloride (NaCl) were supplied by Zhiyuan Reagent Co. Ltd., Tianjin, China. All the materials were used as received without any purification.

Fabrication of the AgNWs and rGO Mixed Suspension: First, AgNO₃ (204 mg) and PVP (399.6 mg) were dissolved in EG (20 mL). The solution was stirred under dark until it was evenly dispersed. NaCl (0.06 mg) was then added into the solution; the mixed solution was heated to 170 °C for 1 h. After removing PVP and EG, AgNWs would be synthesized. Finally, required quantities of rGO were added into AgNWs in ethyl alcohol and the suspension was stirred equably.

Fabrication of the Tunable and Nacre-Mimetic Multifunctional E-Skin: First, 5 g TPU pellets was added into 10 mL DMF and 10 mL THF. One layer of TPU mat was prepared by electrostatic spinning after the solution was completely dissolved. Then AgNWs and rGO mixed suspension were sprayed onto the mat at room temperature. Subsequently, another layer of TPU mat is prepared to cover the conductive layer by electrostatic spinning. E-skin with different properties can be obtained by adjusting the content of rGO and the number of conductive layers.

Characterization: The strain sensitivity of the e-skin was tested on an electronic universal tensile testing machine (model UTM2203, Shenzhen Sun Technology Stock Co. Ltd) and an electrochemical workstation (RST5200, Suzhou Resitest Electronic Co. Ltd., China). The morphology of the e-skin was analyzed using SEM (Zeiss MERLIN Compact), transmission electron microscope (FEI Tecnai G2 F20) and polarization microscope (BX51-PLINKAMTHMS600, Guangzhou Sinoinstrument Co. Ltd.). The thermal stability of the e-skin was tested by TGA (TA Instruments Co., U.S.A.). FTIR measurements were recorded on a Nicolet Nexus 870 instrument (resolution of 4 cm⁻¹ and range of 500–4000 cm⁻¹). Different relative humidity environments (23%, 43%, 67%, and 85%) are prepared by sealing saturated potassium acetate, potassium carbonate, copper chloride, and potassium chloride solutions, respectively. The informed consent was signed by the volunteer for human motion detections experiments. In the test, a piece

of commercial adhesive polyurethane tape was used to separate the volunteer's skin from the multilayered AgNWs/rGO/TPU fibrous mats, which has no physical or psychological effect on the human body. After the experiments, no physical or psychological effect on the volunteer was observed.

Supporting Information

Supporting Information is available from the Wiley Online Library or from the author.

Acknowledgements

The research was financially supported by National Natural Science Foundation of China (51773183, U1804133), National Natural Science Foundation of China-Henan Province Joint Funds (U1604253), Henan Province University Innovation Talents Support Program (20HASTIT001), and Innovation Team of Colleges and Universities in Henan Province (20IRTSTHN002). The authors would like to thank Hou Lijie from Shiyanjia Lab (www.shiyanjia.com) for the TEM analysis.

Conflict of Interest

The authors declare no conflict of interest.

Data Availability Statement

Research data are not shared.

Keywords

contact-noncontact sensing, electronic skin, graphene, nacre-mimetic structure, silver nanowires

Received: January 27, 2021

Revised: April 10, 2021

Published online: June 26, 2021

- [1] S. Wang, J. Xu, W. Wang, G. N. Wang, R. Rastak, F. Molina-Lopez, J. W. Chung, S. Niu, V. R. Feig, J. Lopez, T. Lei, S. K. Kwon, Y. Kim, A. M. Foudeh, A. Ehrlich, A. Gasperini, Y. Yun, B. Murmann, J. B. Tok, Z. Bao, *Nature* **2018**, 555, 83.
- [2] D. Son, J. Kang, O. Vardoulis, Y. Kim, N. Matsuhisa, J. Y. Oh, J. W. To, J. Mun, T. Katsumata, Y. Liu, A. F. McGuire, M. Krasov, F. Molina-Lopez, J. Ham, U. Kraft, Y. Lee, Y. Yun, J. B. Tok, Z. Bao, *Nat. Nanotechnol.* **2018**, 13, 1057.
- [3] T. S. Dinh Le, J. An, Y. Huang, Q. Vo, J. Boonruangkan, T. Tran, S. W. Kim, G. Sun, Y. J. Kim, *ACS Nano* **2019**, 13, 13293.
- [4] K. Zhou, Y. Zhao, X. Sun, Z. Yuan, G. Zheng, K. Dai, L. Mi, C. Pan, C. Liu, C. Shen, *Nano Energy* **2020**, 70, 104546.
- [5] X. Wang, Y. Zhang, X. Zhang, Z. Huo, X. Li, M. Que, Z. Peng, H. Wang, C. Pan, *Adv. Mater.* **2018**, 30, 1706738.
- [6] Y. Yu, G. Zheng, K. Dai, W. Zhai, K. Zhou, Y. Jia, G. Zheng, Z. Zhang, C. Liu, C. Shen, *Mater. Horiz.* **2021**, 8, 1037.
- [7] Z. Zhang, L. Cui, X. Shi, X. Tian, D. Wang, C. Gu, E. Chen, X. Cheng, Y. Xu, Y. Hu, J. Zhang, L. Zhou, H. H. Fong, P. Ma, G. Jiang, X. Sun, B. Zhang, H. Peng, *Adv. Mater.* **2018**, 30, 1800323.

- [8] Z. Han, L. Liu, J. Zhang, Q. Han, K. Wang, H. Song, Z. Wang, Z. Jiao, S. Niu, L. Ren, *Nanoscale* **2018**, *10*, 15178.
- [9] Y. Qiao, Y. Wang, H. Tian, M. Li, J. Jian, Y. Wei, Y. Tian, D. Y. Wang, Y. Pang, X. Geng, X. Wang, Y. Zhao, H. Wang, N. Deng, M. Jian, Y. Zhang, R. Liang, Y. Yang, T. L. Ren, *ACS Nano* **2018**, *12*, 8839.
- [10] S. Chen, Y. Wei, S. Wei, Y. Lin, L. Liu, *ACS Appl. Mater. Interfaces* **2016**, *8*, 25563.
- [11] X. Shi, S. Liu, Y. Sun, J. Liang, Y. Chen, *Adv. Funct. Mater.* **2018**, *28*, 1800850.
- [12] M. D. Ho, Y. Ling, L. W. Yap, Y. Wang, D. Dong, Y. Zhao, W. Cheng, *Adv. Funct. Mater.* **2017**, *27*, 1700845.
- [13] Y. Gao, Q. Li, R. Wu, J. Sha, Y. Lu, F. Xuan, *Adv. Funct. Mater.* **2019**, *29*, 1806786.
- [14] Q. Gui, Y. He, N. Gao, X. Tao, Y. Wang, *Adv. Funct. Mater.* **2017**, *27*, 1702050.
- [15] M. Ha, S. Lim, J. Park, D.-S. Um, Y. Lee, H. Ko, *Adv. Funct. Mater.* **2015**, *25*, 2841.
- [16] Y. Lai, B. Ye, C. Lu, C. Chen, M. Jao, W. Su, W. Hung, T. Lin, Y. Chen, *Adv. Funct. Mater.* **2016**, *26*, 1286.
- [17] W. Zhong, C. Liu, C. Xiang, Y. Jin, M. Li, K. Liu, Q. Liu, Y. Wang, G. Sun, D. Wang, *ACS Appl. Mater. Interfaces* **2017**, *9*, 42058.
- [18] C. Deng, L. Pan, D. Zhang, C. Li, H. Nasir, *Nanoscale* **2017**, *9*, 16404.
- [19] C. Wang, X. Li, E. Gao, M. Jian, K. Xia, Q. Wang, Z. Xu, T. Ren, Y. Zhang, *Adv. Mater.* **2016**, *28*, 6640.
- [20] J. Gao, X. Wang, W. Zhai, H. Liu, G. Zheng, K. Dai, L. Mi, C. Liu, C. Shen, *ACS Appl. Mater. Interfaces* **2018**, *10*, 34592.
- [21] S. Park, J. Kim, M. Chu, M. Khine, *Adv. Mater. Technol.* **2016**, *1*, 1600053.
- [22] I. Kim, K. Woo, Z. Zhong, P. Ko, Y. Jang, M. Jung, J. Jo, S. Kwon, S. H. Lee, S. Lee, H. Youn, J. Moon, *Nanoscale* **2018**, *10*, 7890.
- [23] Y. Jia, X. Yue, Y. Wang, C. Yan, G. Zheng, K. Dai, C. Liu, C. Shen, *Composites, Part B* **2020**, *183*, 107696.
- [24] M. Amjadi, A. Pichitpajongkit, S. Lee, S. Ryu, I. Park, *ACS Nano* **2014**, *8*, 5154.
- [25] J. Oh, J. Yang, J. Kim, H. Park, S. Kwon, S. Lee, J. Sim, H. Oh, J. Kim, S. Park, *ACS Nano* **2018**, *12*, 7546.
- [26] Y. Jeong, H. Park, S. Jin, S. Hong, S. Lee, J. Ha, *Adv. Funct. Mater.* **2015**, *25*, 4228.
- [27] Z. Li, M. Zhu, J. Shen, Q. Qiu, J. Yu, B. Ding, *Adv. Funct. Mater.* **2020**, *30*, 1908411.
- [28] P. Liu, W. Pan, Y. Liu, J. Liu, W. Xu, X. Guo, C. Liu, Y. Zhang, Y. Ge, Y. Huang, *Compos. Sci. Technol.* **2018**, *159*, 42.
- [29] S. Wang, P. Xiao, Y. Liang, J. Zhang, Y. Huang, S. Wu, S.-W. Kuo, T. Chen, *J. Mater. Chem. C* **2018**, *6*, 5140.
- [30] Y. Tai, G. Lubineau, *Adv. Funct. Mater.* **2016**, *26*, 4078.
- [31] Q. Cheng, J. Duan, Q. Zhang, L. Jiang, *ACS Nano* **2015**, *9*, 2231.
- [32] S. Wan, Y. Li, J. Peng, H. Hu, Q. Cheng, L. Jiang, *ACS Nano* **2015**, *9*, 708.
- [33] J. Han, G. Du, W. Gao, H. Bai, *Adv. Funct. Mater.* **2019**, *29*, 1900412.
- [34] S. Borini, R. White, D. Wei, M. Astley, S. Haque, E. Spigone, N. Harris, J. Kivioja, T. Ryhänen, *ACS Nano* **2013**, *7*, 11166.
- [35] J. Zhao, N. Li, H. Yu, Z. Wei, M. Liao, P. Chen, S. Wang, D. Shi, Q. Sun, G. Zhang, *Adv. Mater.* **2017**, *29*, 1702076.
- [36] E. Torres Alonso, D. Shin, G. Rajan, A. Neves, S. Russo, M. Craciun, *Adv. Sci.* **2019**, *6*, 1802318.
- [37] L. Ma, R. Wu, A. Patil, S. Zhu, Z. Meng, H. Meng, C. Hou, Y. Zhang, Q. Liu, R. Yu, J. Wang, N. Lin, X. Liu, *Adv. Funct. Mater.* **2019**, *29*, 1904549.
- [38] Z. Weng, J. Qin, A. A. Umar, J. Wang, X. Zhang, H. Wang, X. Cui, X. Li, L. Zheng, Y. Zhan, *Adv. Funct. Mater.* **2019**, *29*, 1902234.
- [39] A. Smith, K. Elgammal, F. Niklaus, A. Delin, A. Fischer, S. Vaziri, F. Forsberg, M. Rasander, H. Hugosson, L. Bergqvist, S. Schroder, S. Kataria, M. Ostling, M. Lemme, *Nanoscale* **2015**, *7*, 19099.
- [40] W. Xuan, X. He, J. Chen, W. Wang, X. Wang, Y. Xu, Z. Xu, Y. Q. Fu, J. K. Luo, *Nanoscale* **2015**, *7*, 7430.
- [41] D. Zhang, J. Tong, B. Xia, *Sens. Actuators, B* **2014**, *197*, 66.
- [42] J. Yang, R. Shi, Z. Lou, R. Chai, K. Jiang, G. Shen, *Small* **2019**, *15*, 1902801.
- [43] Z. Zhen, Z. Li, X. Zhao, Y. Zhong, L. Zhang, Q. Chen, T. Yang, H. Zhu, *Small* **2018**, *14*, 1703848.
- [44] Y. Yu, Y. Zhai, Z. Yun, W. Zhai, X. Wang, G. Zheng, C. Yan, K. Dai, C. Liu, C. Shen, *Adv. Electron. Mater.* **2019**, *5*, 1900538.
- [45] T. Huang, P. He, R. Wang, S. Yang, J. Sun, X. Xie, G. Ding, *Adv. Funct. Mater.* **2019**, *29*, 1903732.
- [46] H. Liao, X. Guo, P. Wan, G. Yu, *Adv. Funct. Mater.* **2019**, *29*, 1904507.
- [47] J. He, P. Xiao, W. Lu, J. Shi, L. Zhang, Y. Liang, C. Pan, S.-W. Kuo, T. Chen, *Nano Energy* **2019**, *59*, 422.
- [48] H. Zhu, X. Wang, J. Liang, H. Lv, H. Tong, L. Ma, Y. Hu, G. Zhu, T. Zhang, Z. Tie, Z. Liu, Q. Li, L. Chen, J. Liu, Z. Jin, *Adv. Funct. Mater.* **2017**, *27*, 1606604.
- [49] Y. Zhai, Y. Yu, K. Zhou, Z. Yun, W. Huang, H. Liu, Q. Xia, K. Dai, G. Zheng, C. Liu, C. Shen, *Chem. Eng. J.* **2020**, *382*, 122985.
- [50] X. Yu, Y. Li, W. Zhu, P. Huang, T. Wang, N. Hu, S. Fu, *Nanoscale* **2017**, *9*, 6680.
- [51] H. Souiri, D. Bhattacharyya, *ACS Appl. Mater. Interfaces* **2018**, *10*, 20845.
- [52] G. Lu, L. Ocola, J. Chen, *Nanotechnology* **2009**, *20*, 445502.
- [53] G. Lu, L. Ocola, J. Chen, *Appl. Phys. Lett.* **2009**, *94*, 083111.
- [54] T. Fei, K. Jiang, F. Jiang, R. Mu, T. Zhang, *J. Appl. Polym. Sci.* **2014**, *131*, 39726.
- [55] S. Gilje, S. Han, M. Wang, K. L. Wang, R. B. Kaner, *Nano Lett.* **2007**, *7*, 3394.
- [56] I. Jung, D. Dikin, R. Piner, R. , *Nano Lett.* **2008**, *8*, 4283.
- [57] F. Barroso-Bujans, S. Cerveny, A. Alegria, J. Colmenero, *Carbon* **2010**, *48*, 3277.